Spatial distribution of the photopolymerization induced by localized surface plasmons: impact of the morphology of the Au nanoparticles

Amine Khitous, Céline Molinaro, Stephania Abdallah, Minyu Chen, Sylvie Marguet, Guillaume Laurent, Loïc Vidal, Jean-Pierre Malval, Céline Fiorini-Debuisschert, Pierre-Michel Adam, et al.

Spatial distribution of the photopolymerization induced by localized surface plasmons: Impact of the morphology of the Au nanoparticles.

Amine Khitous[1,2], Céline Molinaro[1,2], Stephania Abdallah[1,2], Sylvie Marguet[3], Guillaume Laurent[4], Loïc Vidal[1,2], Jean-Pierre Malval[1,2], Céline Fiorini-Debuisschert[5], Pierre-Michel Adam[6], Ludovic Douillard[5], Renaud Bachelot[6,7,8], Olivier Soppera[1,2*].

[1] Université de Haute Alsace, CNRS, IS2M UMR 7361, F-68100 Mulhouse, France

[2] Université de Strasbourg, France

[3] Université Paris Saclay, CEA, CNRS, NIMBE, F-91191 Gif sur Yvette, France

[4] Université Paris-Saclay, ENS Paris-Saclay, CNRS, PPSM, F-91190, Gif-sur-Yvette, France.

[5] Université Paris Saclay, CEA, CNRS, SPEC F-91191 Gif sur Yvette, France

[6] Light, nanomaterials, nanotechnologies (L2n) Laboratory, CNRS UMR 7076. University of Technology of Troyes, 12 rue Marie Curie, F-10004 Troyes Cedex, France

[7] CNRS-International-NTU-Thales Research Alliance (CINTRA), 50 Nanyang Drive, Singapore 637553, Singapore

[8] Sino-European School of Technology, Shanghai University, Shanghai, PR China

* Contact: olivier.soppera@uha.fr

Abstract

The analysis of the local distribution of the electric field, induced by localized surface plasmon resonance (LSPR), is crucial for selecting the morphology of gold nanoparticles (AuNPs) for specific applications. The reported study is based on LSPR-induced near-field two-photon photopolymerization (NF2P) reaction. The initiation of NF2P is triggered by LSPR enhanced near-field light, while in the far-field, oxygen inhibits this reaction. The spatial extend of NF2P reaction is compared to the local electric field distribution depending on AuNP morphologies, established by numerical simulations. Overall, our results demonstrate that the photopolymerization is not only driven by the local near-field enhancement but also strongly depends on the topologies of nanoobject and

photopolymerization extend was more confined in anisotropic and sharp structures compared to isotropic ones. Additionally, we showcased its capability to confine polymerization reactions within nanoscale volumes, with the possibility of controlling the localization of polymer lobes at a single triangle apex, for instance, via light polarization.

Keywords: localized surface plasmon resonance, near-field photopolymerization, electric field localization, two-photon polymerization.

Introduction

Plasmonics has proven to be a real source of innovation in fields as diverse as medicine[1,2], photocatalysis[3,4], electronics[5,6] and detection[7,8]. Localized surface plasmon resonance is influenced by a variety of parameters[9] such as the nature of the metal[10], the dielectric environment[11] and the shape of the particles[12]. Much theoretical research has focused on these crucial aspects[13–17]. Excitation and decay of localized surface plasmons produces three remarkable effects[18]: near-field light enhancement, hot electron transfer, and thermal effects[19–24]. A major challenge today is to be able to take profit of these effects to induce chemical reactions and control their spatial extend at the nanometer scale.

The near-field description of the plasmon-matter interaction at the nanometer scale therefore seems to be a major challenge, justifying the different approaches of photochemical near-field imaging developed in recent years[18,25,26]. The first proof of concept was shown with photoisomerisable polymers[27]. Briefly, near-field light enhancement causes isomerization of azobenzene, leading to migration of the material under the gradient of light intensity[23,26,28]. Field map was then visualized through induced topography monitored by atomic force microscopy (AFM).

In parallel with this approach, near-field polymerization has shown interest both in elucidating fundamental phenomena and in moving toward applications in photonics or photocatalysis[11,19,25]. Near-field polymerization can occur through either electrochemical process[27,28], facilitated by hot electron transfer, or photon-induced mechanisms[19,22], driven by enhanced absorption of near-field light. The goal is to take a snapshot of the near-field during irradiation, assuming that the polymer formed corresponds to the zone where the field was locally enhanced. It can be analyzed by various microscopy techniques such as AFM or scanning electron microscopy (SEM).

Currently, most metallic nanoparticles (MNPs) used or studied in the literature are synthesized colloidally[29]. This synthesis method offers precise, roughness-free geometry control of MNPs, in contrast to substrate-based nanostructure fabrication by electron beam lithography (EBL). Up to now, most studies that have used chemistry to map electric field distribution have used MNPs synthesized by EBL[22–24,30,31]. In addition, the use of AFM as an observation method makes the effect of shape less straightforward to analyze. Recently, new approaches have been proposed, including the deposition of colloidal MNPs on substrates and the observation of near-field polymerization by transmission electron microscopy (TEM)[19,25] or SEM[22,32].

In this study, we relied on an approach recently developed by Kameche et al.[19]. Plasmon-assisted nanophotopolymerization was carried out directly on TEM grids (Si_3N_4 thin film substrates), allowing us to experimentally study, via high resolution TEM imaging, the shape-dependent distribution of polymer around colloidal Au nanoparticles (AuNPs). The advantage of this approach is that NPs can be observed at the end of the different stages. A large number of NPs are deposited on the grid, enabling the selection of objects with identical geometries, which are verified by TEM. Here, near-field two-photon photopolymerization (NF2P) was used. To this end, NF2P is systematically applied to AuNPs of different morphologies under controlled irradiation conditions, including polarization. The distribution of the polymer was observed by TEM and its spatial distribution around AuNPs was compared with near-field maps derived from numerical simulations. The aim is to determine the conditions that allow localization and confinement of the polymerization reaction at the nanometer scale. This is of interest not only on a fundamental scale to improve our understanding of plasmon-matter coupling, but also for applications in nanophotolithography and the fabrication of hybrid nanoparticles (metal-polymer) with control over the positioning and size of the polymer patches.

In the following, we describe the method used to deposit AuNPs on the TEM grid, the photopolymerizable formulation used, and the different AuNP shapes used. Finally, the polymer distributions around the AuNPs are compared with the electromagnetic field maps to discuss the agreement between the two and, more generally, to discuss photopolymerization processes at the nanometric scale.

Methods

Synthesis of AuNPs: The AuNPs used were prepared by colloidal synthesis in aqueous solution. Four types of objects were used in this study: Au nanodisks (AuNDs), Au

nanohexagons (AuNHs), Au nanorods (AuNRs) and Au nanotriangles (AuNTs). For the synthesis of disks, hexagonal and triangular nanoparticles, nanoplates with a thickness of 15 nm (comprising a mixture of triangular and hexagonal shapes) were initially prepared. Subsequently, AuNDs were obtained through mild oxidation of these hexagonal plates, following our previously published protocol[33]. The AuNRs were synthesized according to the protocol specified in the reference[34,35]. Synthesis methods are chosen to generate AuNPs that are monodisperse in size. In our approach, TEM is used to verify that the nano-objects selected for photopolymerization are of the correct size. For AuNDs, a diameter of 80 ± 5 nm with a thickness of 13 ± 2 nm, checked by AFM, was targeted. For AuNHs, the NP edge is 80 ± 5 nm and the height is 15 ± 2 nm. Reference AuNRs have a diameter of 25 ± XX nm and a length of 75 ± 12 nm. On these objects, other dimensions and shapes are used and mentioned in this case (AuNRs: 22.5 nm x 65 nm; 27 nm x 75 nm and 32 nm x 85 nm). Finally, AuNTs are 75 ± 15 nm in edge with a thickness of 15 ± 2 nm. These dimensions were chosen to enable a plasmon resonance at a wavelength of 800 nm. Simulated scattering, absorption and extinction spectra of these AuNPs are shown in **Figure S1**.

Deposition of AuNPs: The aim here is to study the response of individual AuNPs. The different types of AuNP are deposited on a TEM grid with a low concentration to avoid any coupling between NPs. This grid consists of two rectangular windows (1500 µm × 100 µm) covered with a 50 nm thick Si_3N_4 membrane (Ted Pella Inc.). Surfactant (cetyltrimethylammonium bromide – CTAB) is removed from colloidal solutions by dilution and centrifugation.

After AuNP deposition, the TEM grid was exposed to UV-ozone (Bioforce Procleaner Plus UV) for 2 h and then rinsed with deionized water. The absence of surfactant on the edges of the NPs was verified by TEM (ARM200F JEOL high-resolution transmission electron microscope) as shown in **Figure 1**. Due to shading effect, the surfactant is still present under the NPs. For this reason, an organic layer of 1 nm (typical thickness of such self-assembled monolayer) between the NPs and the Si_3N_4 substrate was considered for numerical simulation. Preliminary experiments were conducted to check that no topological changes in the polymer lobes were induced during analysis due to the e-beam probe. To this end, images of AuNPs were compared at different e-beam exposure times. The results showed excellent stability of the hybrid nanoparticles with the TEM imaging conditions. Interestingly, the hybrid NPs showed a remarkable stability, with same structure of both metal and polymer parts after several weeks.

The direction of the electron beam in the TEM is identical to that of the light propagation used to irradiate the NPs (surface normal). This direction is also used in simulations. TEM observations thus correspond to the projection in the substrate plane, e.g. perpendicular to the direction of light propagation.

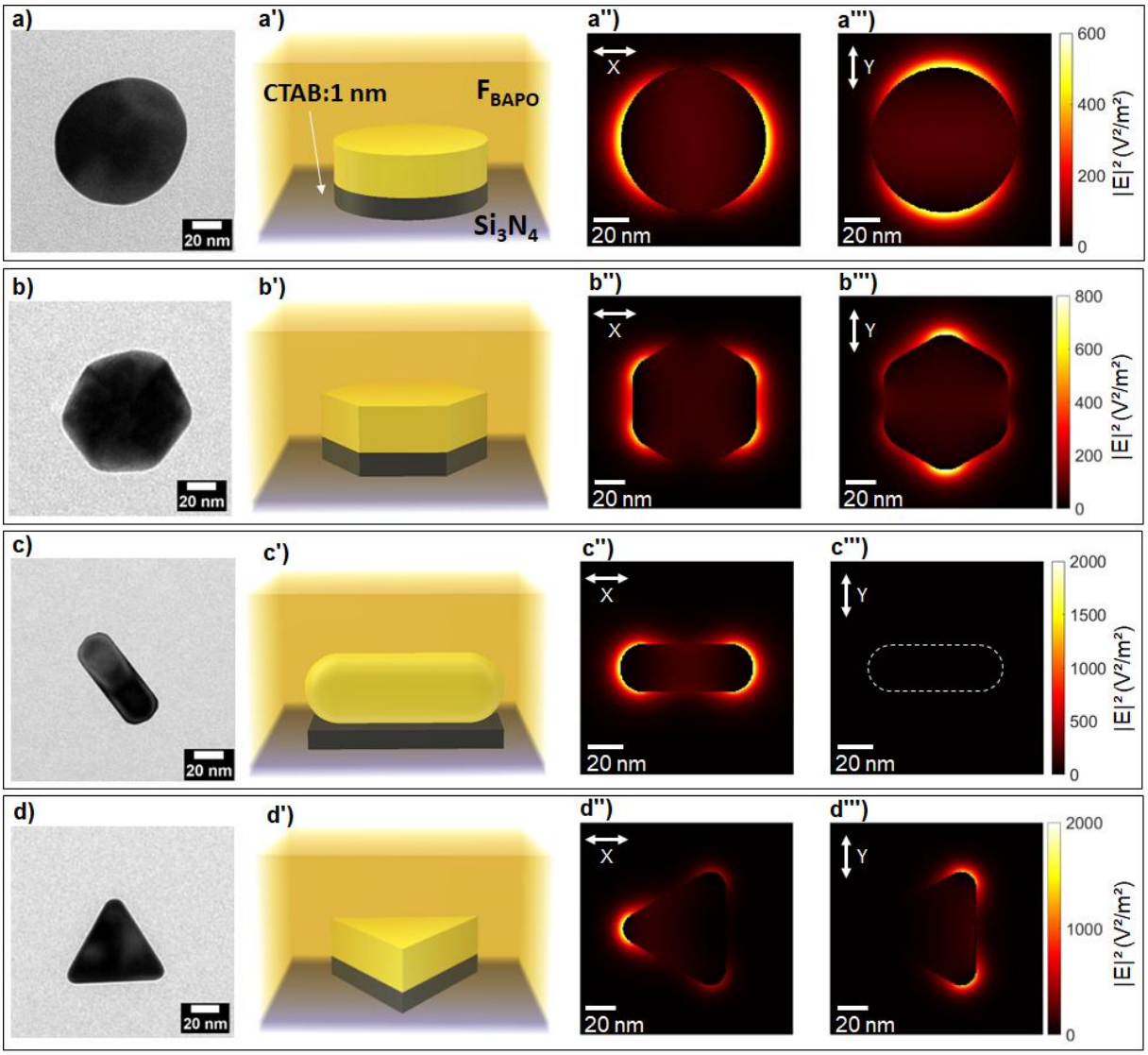

Figure 1: TEM images of AuNDs (**a**), AuNHs (**b**), AuNRs (**c**) and AuNTs (**d**). 3D schematic representation of the different NP structures in which AuNDs (**a'**), AuNHs (**b'**), AuNRs (**c'**) and AuNTs (**d'**) are deposited on the Si_3N_4 substrate (refractive index (RI): 2.02), considering a remaining layer of CTAB (thickness: 1 nm, RI: 1.48), and a surrounding by the photopolymerizable formulation (F_{BAPO}, RI: 1.48). Field intensity map under X polarization: AuNDs (80 nm) (**a''**), AuNHs (80 nm) (**b''**), AuNRs (27 nm x 75 nm) (**c''**) and AuNTs (75 nm) (**d''**). Field intensity map under Y polarization: AuNDs (80 nm) (**a'''**), AuNHs (80 nm)

(**b''**), AuNRs (27 nm x 75 nm) (**c''**) and AuNTs (75 nm) (**d''**). Excitation at 800 nm wavelength under normal incidence.

Photopolymerizable formulation: The formulation used in this study comprises phenyl bis(2,4,6-trimethylbenzoyl) phosphine oxide (BAPO, Sigma Aldrich) as photoinitiator (PI) and pentaerythritol triacrylate (PETA) as monomer (**Figure S2**). BAPO is a PI that exhibits single-photon absorption in the wavelength range between 360 and 400 nm. It is used here as a two-photon photoinitiator[36] using a laser delivering femtosecond pulses at 800 nm (Ti:Sapphire mode-locked oscillator Coherent, Chameleon Ultra II) with a pulse duration of 150 fs and a repetition rate of 80 MHz.

Exposure conditions: Once the AuNPs are deposited on the TEM grid, the grid is mounted on a glass slide. Next, a drop of the BAPO formulation (F_{BAPO}) is deposited on the grid, and the whole assembly is mounted on a 3D piezoelectric stage that allows the sample to be moved laterally in the laser focus. All sample movements and light parameters such as excitation power and exposure times are computer controlled. Irradiation is performed with a 3D lithographic microfabrication tool using a Zeiss Axio Observer D1 inverted microscope. Irradiation is performed at constant time and variable power under normal incidence. It is important to note that the laser used is linearly polarized. The incident beam is focused through a 0.95 NA (×40) objective, inducing a spot with an estimated diameter of 1.2 ± 0.3 µm at the excitation wavelength of 800 nm. The beam scans the surface of the sample at a lateral speed of 10 µm/s and the exposure time is set to 100 ms. The dose received at each point is modulated by changing the laser power using an acousto-optic modulator.

Photopolymerization threshold dose: Determination of the photopolymerization threshold dose (D_t) is a prerequisite for near-field experiments. This D_t represents the energy required to initiate the far field photopolymerization reaction at the focal point (2F2P). It is determined by depositing a drop of F_{BAPO} on the TEM grid and irradiating it in the absence of AuNPs by modulating the incident power. In practice, D_t is measured by tracing polymer lines on the substrate with laser beam at a speed of 10 µm/s. D_t was measured at 71.3 kJ/cm² on the TEM grid.

Once D_t is determined, F_{BAPO} is deposited on TEM grids with AuNPs and irradiated at doses below the threshold dose, expressed as % of D_t. After irradiation, the TEM grid is immersed in an acetone and ethanol bath to remove any unpolymerized formulation and then carefully dried before observation.

For each chosen dose, a minimum of 4 comparable particles were imaged by TEM (**Figure S3-S6**). Below, a representative image is shown and the thickness of the polymer layer is evaluated using ImageJ software on an average of 5 different particles. Error bars are deduced from the standard deviation of thickness measurements. Note that verification experiments were performed to ensure that unreacted photopolymer was perfectly removed from the substrate and that AuNPs did not move on the TEM grid surface throughout the procedure. Thanks to the different TEM contrasts between the metal NPs and the polymer, it is possible to precisely determine the NP cross-section in the plane of the substrate, and to verify their characteristic sizes and shapes, which is another advantage of the method used in this work.

Simulations: The absorption, scattering, extinction cross sections and field maps presented here were obtained by numerical simulations using the MATLAB toolbox Metallic Nanoparticles Boundary Elements Method (MNPBEM, version 17)[37,38]. In order to be as close as possible to the experimental values, numerical simulations were performed for the following AuNPs: AuNDs (diameter 80 nm, thickness 13 nm), AuNHs (edge 80 nm, thickness 15 nm, radius of curvature of apexes 9 nm), AuNRs (22.5 nm x length 65 nm, 27 nm x 75 nm, 32 nm x 85 nm), and AuNTs (edge 75 nm, thickness 15 nm, radius of curvature of apexes 17 nm). For each AuNP, simulations were performed considering a single AuNP in a medium of refractive index RI = 1.48 (corresponding to the index of F_{BAPO}). This particle is located 1 nm above the substrate (corresponding to the thickness of the remaining CTAB under the AuNPs). The substrate with RI = 2.02[39] is considered infinite. The refractive index of Au is taken from Johnson and Christy[40]. The AuNP is illuminated from the substrate under normal incidence with linear polarization whose in-plane angle can be adjusted. All simulations are performed in retarded mode. The field maps have been generated with illumination at 800 nm wavelength. All maps show the squared modulus of the electric field; top view in the equatorial plane of each AuNP.

Results & Discussion

Investigation of the distribution of near-field light enhancement by NF2P

Figure 2 summarizes the principle of the experiments at molecular and nanometer scales. By irradiating AuNPs immersed in the photopolymerizable formulation under $D < D_t$ of 2F2P, photopolymerization cannot be induced without interaction with the nanoparticles. The absence of 2F2P under $D < D_t$ can be explained by the existence of an inhibition pathway that annihilates the excited stated of the PI and the first radicals formed. Oxygen dissolved in the

medium plays this role under our conditions, as shown in **Figure 2.** R° radicals react with oxygen to form peroxide radicals, which are inactive for radical polymerization[41].

On the other hand, in the vicinity of AuNPs, the enhancement of the electromagnetic field allows D_t to be locally exceeded. Thus, in these zones, polymerization can become competitive with inhibition and the polymerization reaction occurs quantitatively enough for polymer to be observable after development.

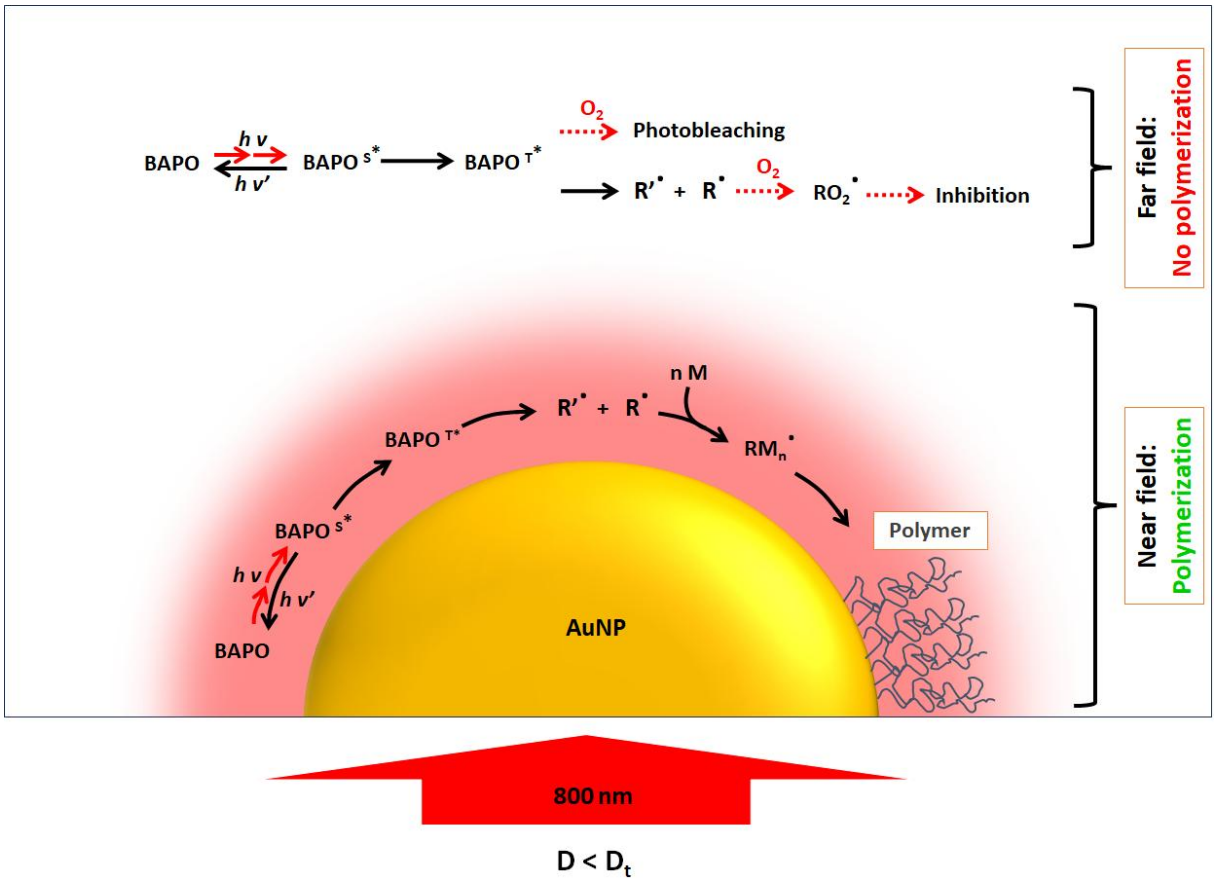

Figure 2: Schematic of NF2P: for $D < D_t$, NF2P is only triggered on the surface of AuNPs through light enhancement in near field. In far field, the presence of oxygen inhibits the 2P reaction due to low irradiation energy.

This method should not only reveal the near-field enhancement, but also characterize its spatial confinement, assuming that the polymerization reaction is itself confined. By staying sufficiently far away from D_t, we can limit the concentration of radicals formed, which a priori limits the spatial extent of the polymerization. Indeed, just as primary radicals formed far from the Au surface are consumed by oxygen, the propagation of radical polymerization away from the Au surface is limited by the same inhibition reaction.

In the following, we consider the four types of nano-object presented in the experimental section to investigate how NF2P follows field profiles. This study also allows us to compare the nano-objects with each other. The objects were chosen to have a resonance around the irradiation wavelength used (800 nm). The effective cross-sections (shown in **Figure S1**) show different values between the different objects. The field intensities are also very different, as shown in **Figure 1**.

As previously stated, depending on the experimental conditions, there are three possible explanations for the polymerization mechanism observed here. Purely thermal polymerization was ruled out by experiments showing that monomer without photoinitiator did not polymerize under the conditions used in this study. As for the contribution of hot carriers, although not completely excluded, the near-field polymerization thresholds are consistent with the far-field polymerization thresholds corrected for the exaltation factor. Moreover, polymerization of the monomer without initiator is not observed under these power conditions, which means that the polymerization is triggered by a mechanism implying the BAPO. In our conditions, the BAPO photoinitiator is diluted in the monomer at a concentration of 36 mM, which corresponds to 15 BAPO molecules in the polymerized volume. This concentration is extremely low which makes it very unlikely to initiate a polymerization reaction via electron transfer. Indeed, such process requires an electron acceptor species in the surrounding medium, in high concentration and close vicinity to the metal surface since the charge transfer can only occur at short distance and before electron thermalisation. In literature, ionic polymerization processused NPs covered by a layer of electron acceptors. [24] In our conditions, the evanescent wave penetration depth (12 nm) appears suitable to trigger the polymerization by photochemical process.

Nanodisks (AuNDs)

AuNDs are considered first. As shown in **Figure 1**, they are the objects with the lowest field intensity (600 V^2/m^2) among the nano-objects tested (pole plasmon resonance). Note that the AuNDs presented here have a resonance around 750 nm. Their symmetry results in a response that follows the polarization direction of the incident field. AuNDs were irradiated at different doses below D_t (between 8.5% and 35.5% D_t for the whole study) according to the protocol described above. TEM images of AuNDs after irradiation and rinsing are shown in **Figure 3**.

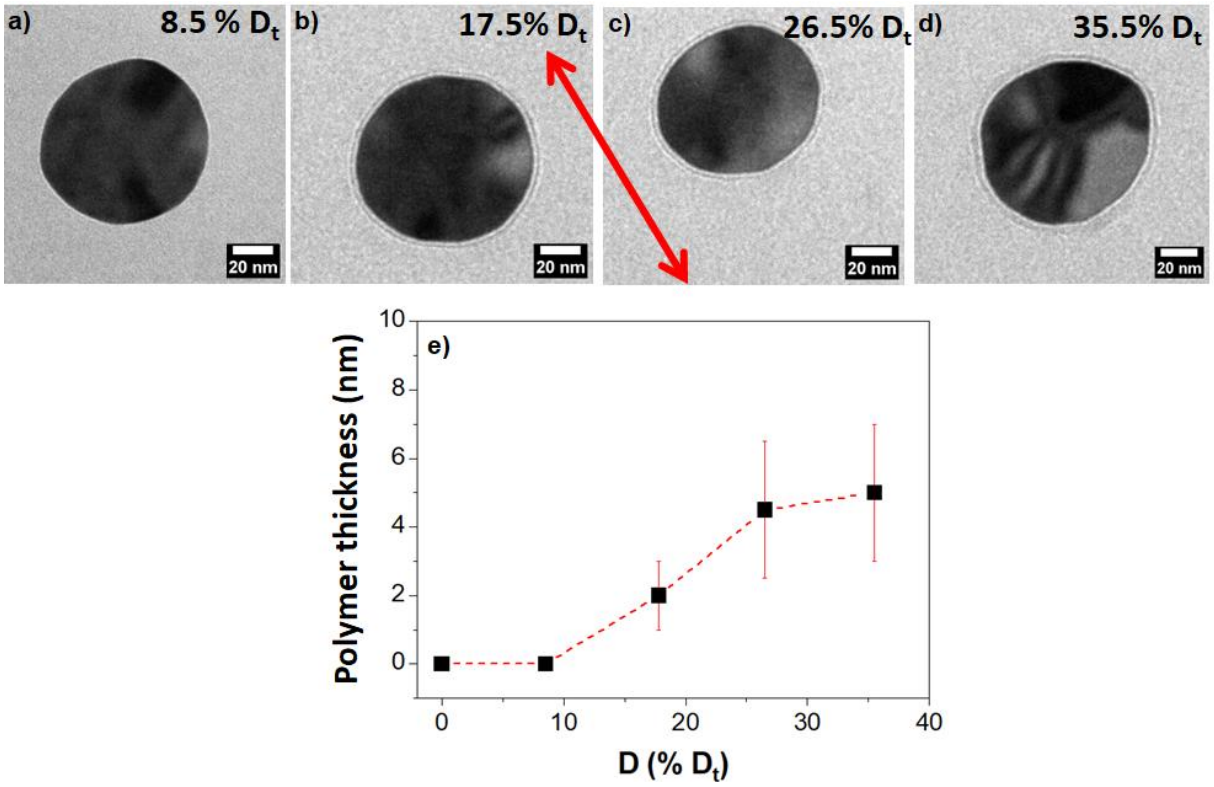

Figure 3: Effect of dose on NF2P on AuNDs, TEM imaging: (**a**) 8.5% D_t, (**b**) 17.5% D_t, (**c**) 26.5% D_t, (**d**) 35.5% D_t, and (**e**) variation of the near-field polymer thickness as a function of irradiation power (%D_t). The red arrow indicates the light polarization.

Irradiation of AuNDs at 8.5% D_t did not reveal the presence of polymer, indicating that the polymerization threshold was not reached (**Figure 3.a**). In addition, we verify in this image that the method of rinsing the AuNDs with ethanol and acetone completely eliminates the unreacted F_{BAPO}.

The NF2P was observed around the AuNDs starting at 17.5% D_t, with a gradually increasing thickness to reach 5 nm at 35.5% D_t (**Figure 3.b-e**).

In these experiments, the light is linearly polarized in the direction of the red arrow in **Figure 3**. The simulations in **Figure 1.a** show an anisotropic distribution of the electric field on the surface of the AuNDs, with regions of maximum exaltation in the direction of polarization. For all doses, polymerization is observed homogeneously over the entire circumference of the AuND.

This result is therefore surprising and contradicts the results of Ge et al.[32] who observed an anisotropic distribution of polymer around circular nanostructures. It should be noted that in this study the AuNPs were larger (disk diameter ≈ 100 nm) and prepared by electron beam

lithography[32]. This difference will be discussed further after analyzing the results of other shapes of AuNPs.

Nanohexagons (AuNHs)

As shown in the field maps in **Figure 1**, maximum of field intensity is expected at the apexes of the hexagon. The amplitude and the distribution of the field are slightly different depending on the polarization direction of the incident light. The field intensity is more important than in the case of AuNDs. The NF2P results of AuNHs are shown in **Figure 4**.

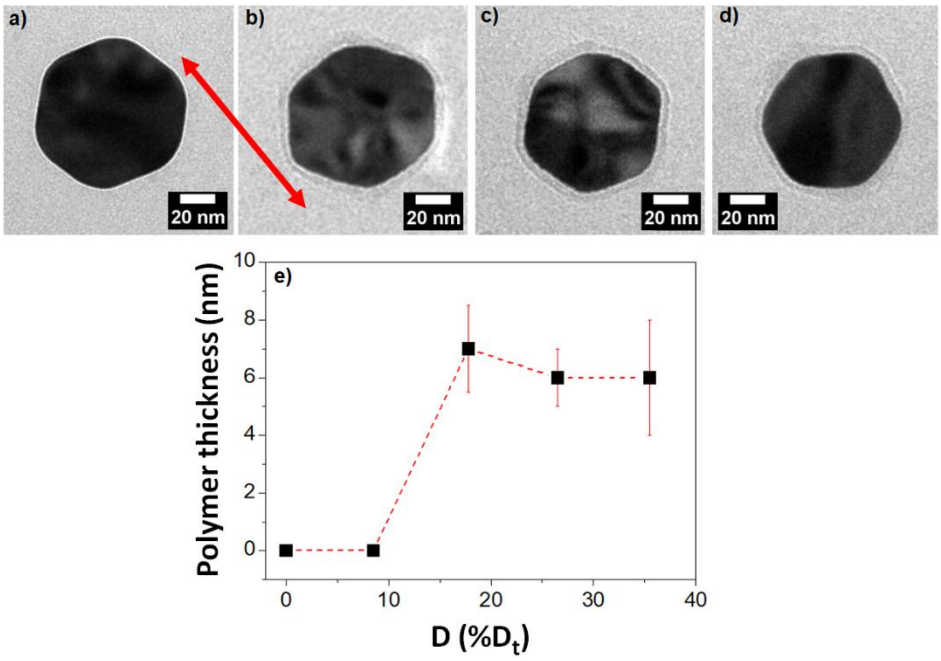

Figure 4: Effect of the dose on NF2P on AuNHs (75 ± 10 nm), TEM imaging: (**a**) 8.5% D_t, (**b**) 17.5% D_t, (**c**) 26.5% D_t, (**d**) 35.5% D_t, and (e) the variation of near-field polymer thickness as a function of irradiation power. The red arrow denotes light polarization.

As for AuNDs, no NF2P was observed for AuNHs at 8.5% D_t (**Figure 4.a**). Photopolymerization is observed from 17.5% D_t, demonstrating that the enhancement around the AuNHs makes it possible to initiate the reaction in the near field. As with AuNDs, polymerization is not localized, but a polymer layer is observed all around the AuNHs. At higher doses, the thickness of the polymer in the near field remains around 6 nm (**Figure 4.b-e**). Thus, the reaction is well confined at the NP surface. This result confirms the simulations that show a very strong decrease in the intensity of the evanescent field as the distance from the NP increases.[39] Note that this thickness, like all those reported in this work, is much smaller than that obtained in the SPR configuration on continuous Au films[43-45].

As can be seen from the TEM images, the radii of curvature at the apexes of the AuNHs are relatively large, which can explain that the spatial distribution of the polymer around the AuNHs is close to that observed on the AuNDs. However, a closer look at some particles shows a slight difference in the thickness of the polymer layer between the polarization direction and the perpendicular direction. For instance, in **Figure 4.c**, the thickness is 6 nm in the polarization direction and 4 nm in the perpendicular direction (see also zoom in **Figure S7**). This difference in thickness in both directions is small, but it has been observed on several nanohexagons, which is why we report the results here. It is noted that the polarization in this case is across the edges of the hexagon, and the polymer is localized on these two edges thus following the electric field intensity depicted in **Figure 1**. However, in the case where the polarization is across two apexes, the polymer is more localized on these two apexes exactly as shown in **Figure 1**. The field distributions correspond to the expected plasmon eigenstates of dipolar character for a particle of hexagonal symmetry [33].

To further investigate the effect of shape on the spatial localization of photopolymerization, we consider then nanorods.

Nanorods (AuNRs)

As shown in the field maps in **Figure 1**, the topology of the nanorods induces a very different response depending on the angle between the AuNR and the polarization direction of the light. The irradiation of AuNRs at different doses is shown in **Figure 5**. AuNRs oriented in a direction close to the polarization direction were used in this part.

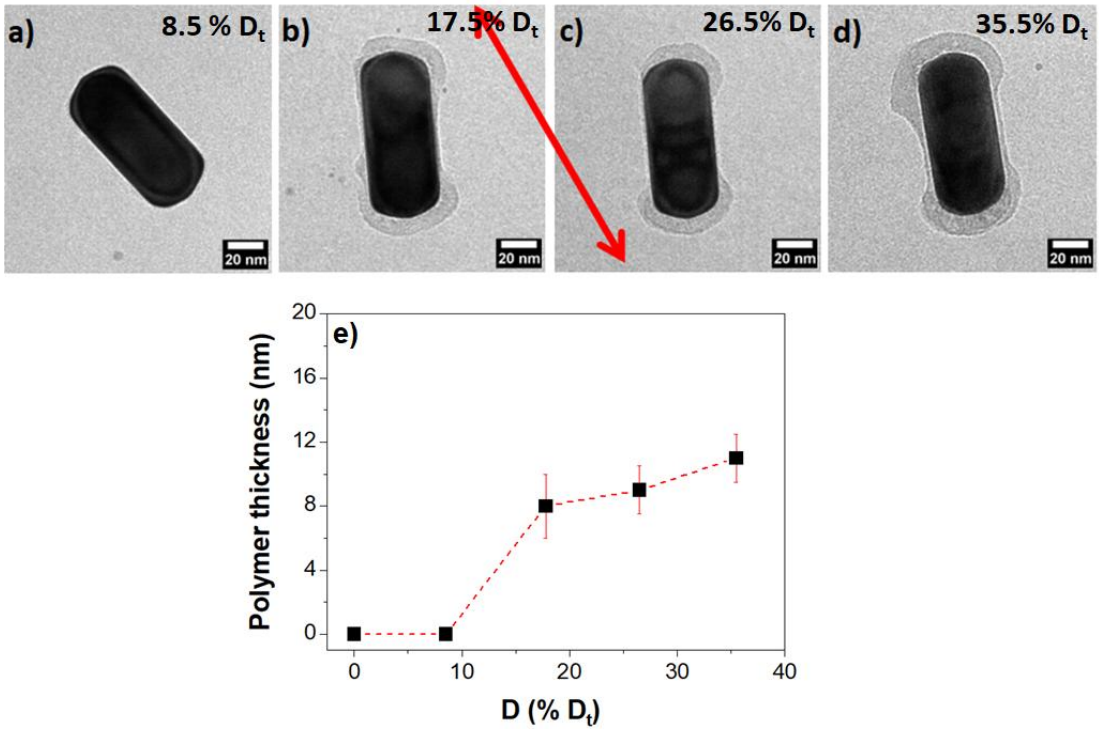

Figure 5: Effect of dose on NF2P on AuNRs, TEM imaging: (**a**) 8.5% D_t, (**b**) 17.5% D_t, (**c**) 26.5% D_t, (**d**) 35.5% D_t, and (**e**) variation of near-field polymer thickness as a function of irradiation dose. The red arrow indicates light polarization.

As for the other two types of nanoobject, at 8.5% D_t, no polymer was observed in the near field (**Figure 5.a**). From 17.5% D_t, the NF2P is observed. The thickness of the polymer increases slightly with irradiance between 17.5% and 35.5% D_t, reaching a thickness of 12 nm (**Figure 5.b-e**), twice that observed for AuNDs and AuNHs (**Figure 3** and **Figure 4**).

Regarding the spatial distribution of the polymer, it is clearly localized at the ends of the AuNRs when they are irradiated with a polarization aligned with their long axis. Comparing the field maps shown in **Figure 1**, we conclude that for AuNRs, unlike AuNDs and AuNHs, there is a much better correlation between the near-field distribution and polymerization zones.

As for the effect of the orientation of the AuNRs with respect to the polarization of the light, this property is well verified by studying the effect of the orientation of the AuNRs with respect to the in-plane polarization direction of the light. Differently oriented AuNRs were irradiated by fixing the polarization direction. The results are shown in **Figure 6**.

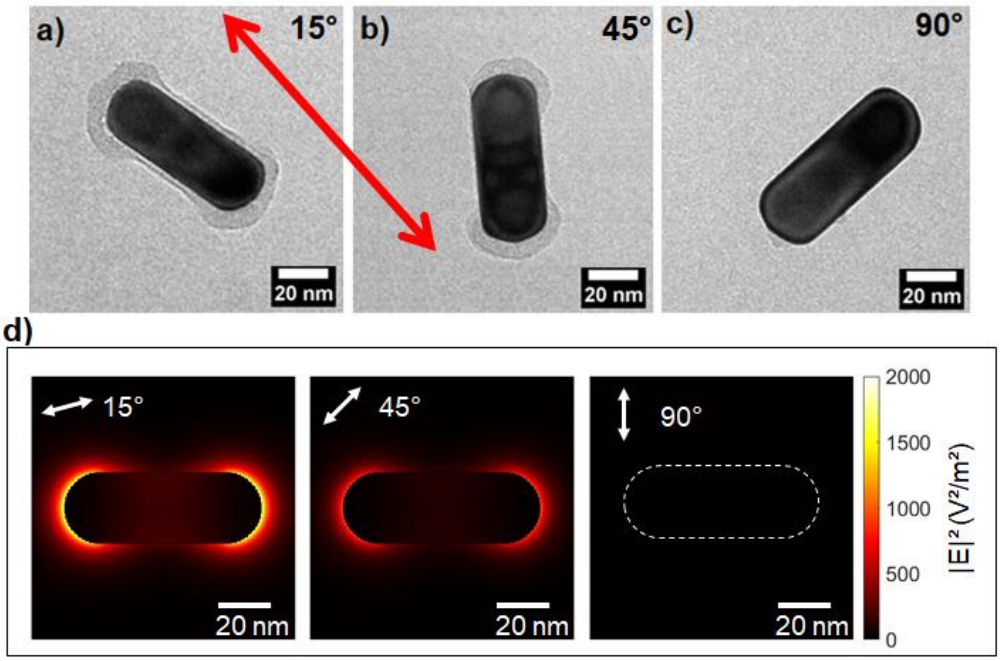

Figure 6: Influence of the angle between the AuNR longitudinal axis and the in-plane polarization direction on NF2P, TEM imaging. 15° (**a**), 45° (**b**) and 90° (**c**), irradiance: 26.5% D_s. The red arrow indicates the in-plane direction of light polarization.. (**d**): $|E|^2$ map of AuNRs (27 nm x 75 nm) as a function of the incident polarization angle, numerical simulation. Excitation at 800 nm, normal incidence.

From **Figure 6.c** it is clear that when the light is polarized along the transverse axis of the AuNR, no polymerization is obtained, which is consistent with the simulations presented in **Figure 1**. In fact, the transverse mode cannot be excited because it corresponds to a resonance at 532 nm (**Figure S1**). However, as shown in **Figure 6.a** and **Figure 6.b**, when the light polarization is parallel to the longitudinal axis or tilted (up to 60°), the NF2P is triggered. To better understand this aspect, the field intensity was simulated as a function of the tilt angle between the longitudinal axis and the polarization of the light. **Figure 6.d** shows that the field intensity decreases with increasing angle until it disappears for an angle of 90° (**Figure S8**). On the other hand, the AuNR tilted by 45° shows a better localization of the NF2P compared to the AuNR parallel to the polarization, this is due to the weak exaltation in the center of the AuNR (**Figure S8.b**). This suggests that the polarization of the incident light allows anisotropic control of the functionalization of nanostructures[47].

Finally, the effect of the volume of the AuNRs was studied. We studied 3 AuNRs of distinct volumes with the same spectral position of the longitudinal resonance (around 800 nm). Their respective form factors were validated by BEM simulation to maintain a unique longitudinal

resonance. (**Figure S1.d-f**). The images in **Figures 7.a-c** show that NF2P is effective for all 3 types of AuNRs. We observe a significant difference in the distribution of the polymer around the AuNRs: the polymer is more localized on the AuNRs with the most distant ends. As the ends get closer, more polymer is present in the middle part of the AuNR. This result should be compared with the field maps generated for the 3 AuNRs (**Figure 7.d-g**).

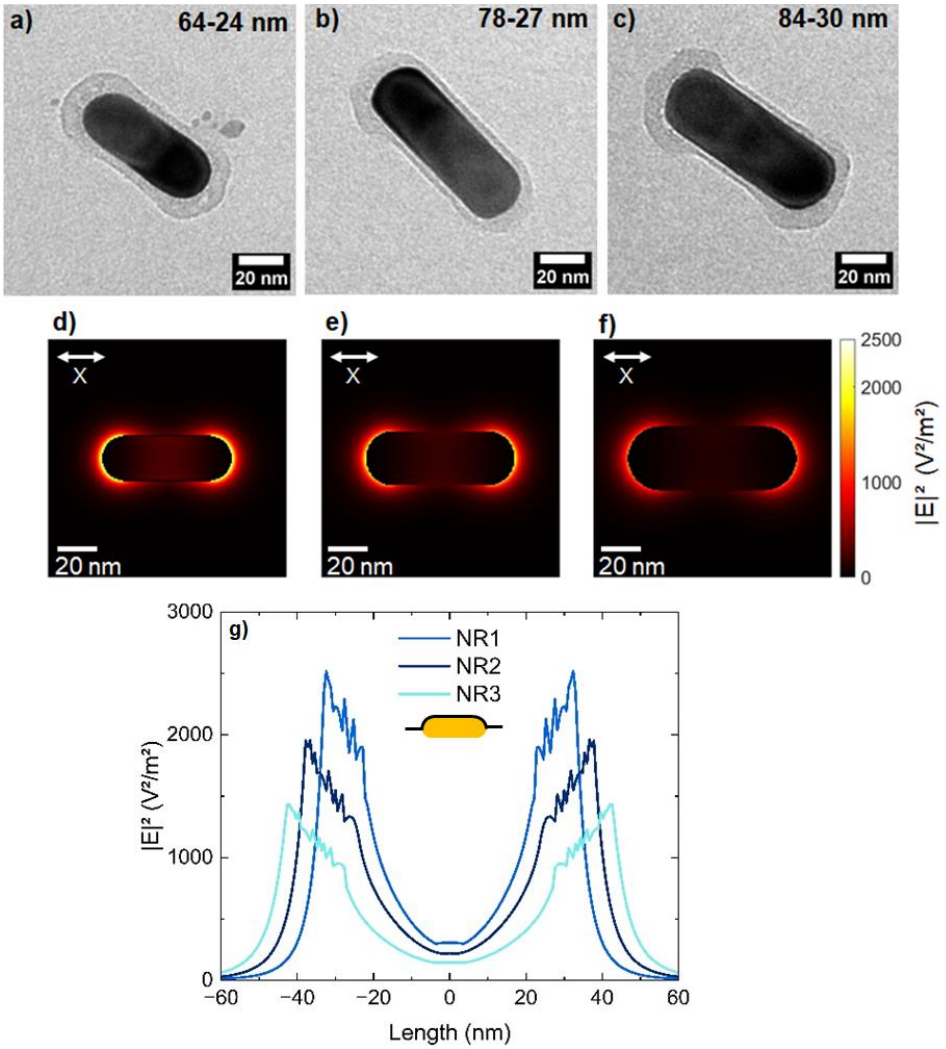

Figure 7: Effect of size (**a-c**) of AuNRs on NF2P, TEM imaging: 17.5% D_t. The red arrow denotes light polarization (pas présente). $|E|^2$ maps of AuNRs, of various sizes, excited by X longitudinal polarization at 800 nm: 22.5 nm x 65 nm (**d**), 27 nm x 75 nm (**e**), 32 nm x 85 nm (**f**) and Field intensity ($|E|^2$) profiles for the 3 AuNRs along the object perimeters (**g**).

By analyzing the field intensity maps and profiles along the AuNRs (**Figure 7.d-g**), it is observed that the smaller the AuNR (smaller end curvature radii), the higher the field intensity at the ends and in the middle of the particle. For given irradiation conditions, this property increases the probability of radical formation in the intermediate zone. At the same time, the

probability of consuming oxygen in the center of the NP increases, and ultimately the probability of triggering the NF2P also increases.

Nanotriangles (AuNTs)

AuNTs appear as a complementary and interesting shape due to the possibility of selectively enhancing the near field at one or two apexes, depending on the direction of polarization relative to the axis of the triangle [48] (**Figure 1**). The simulated spectra are shown in **Figure S1**. The results of the NF2P study on AuNTs are shown in **Figure 8**.

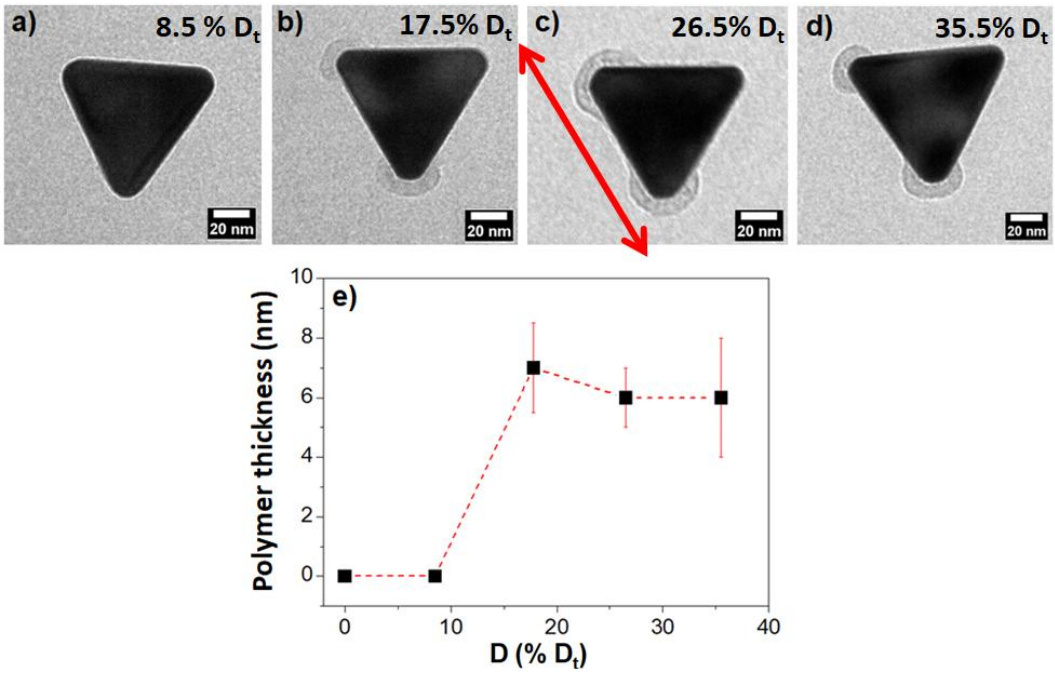

Figure 8: Effect of dose on NF2P on AuNTs of the same size (equilateral triangle of 75 ± 15 nm edge size), TEM imaging: (**a**) 8.5% D_t, (**b**) 17.5% D_t, (**c**) 26.5% D_t, (**d**) 35.5% D_t, and (**e**) variation of near-field polymer thickness as a function of dose. The **red arrow** indicates the direction of polarization.

As for the previously studied forms, near field polymerization is not observed for 8.5% D_t in the case of AuNTs (**Figure 8.a**). NF2P is initiated at 17.5% D_t. From this dose, the size of the polymer lobes remains constant around 6 nm.

Regarding the localization of the polymerization, the NF2P was clearly anisotropic and localized at the two excited apexes, which are on the edge aligned on the polarization. The study of the effect of the polarization orientation showed that it is possible to localize the NF2P on a single apex when the polarization is parallel to the in-plane triangle height, or on

two apexes when the polarization is parallel to the edge (**Figure 9**). This location correlates well with the field maps shown in **Figure 1** and correspond to the two in-plane resonance eigenvectors of a triangle[48].

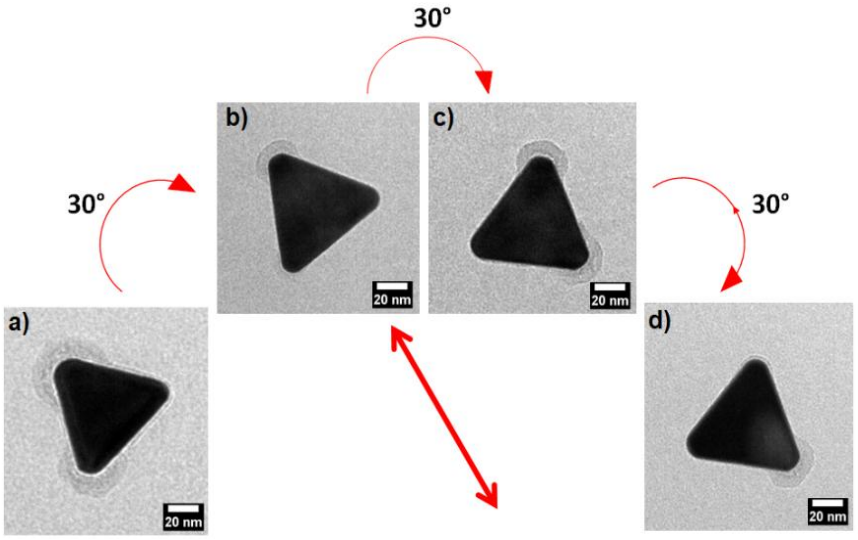

Figure 9: TEM images depicting the effect of AuNTs (75 ± 15 nm nm) orientation relative to light polarization (**red arrow**): 17.5% D_t.

Although AuNTs show high field intensity (**Figure 1**), the small size of the polymer lobes obtained here compare to those obtained with AuNRs. This can be explained by the extreme confinement of the enhanced field zone in the case of AuNTs (small curvature radii at corner positions). Thus, the production of radicals is effective in this volume, and the propagation of the radical polymerization reaction beyond this volume is limited by the inhibition reactions, which ultimately confine the polymerized volume.

To explain the location of the NF2P, we have plotted the distribution of field intensities around the different AuNPs (shown on the same scale in **Figure 10**).

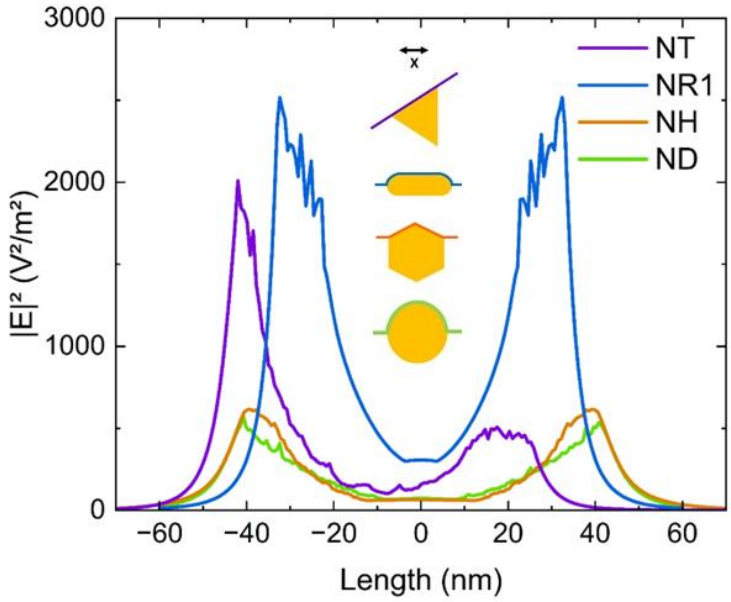

Figure 10: $|E|^2$ contours of AuNTs, AuNRs, AuNHs and AuNDs along the segments shown in the diagrams on the right. Excitation at 800 nm and polarization in X direction.

According to **Figure 10**, the most localized and effective NF2P correspond to the strongest and most localized exaltation effects (small curvature radii at corner, resp. end positions). The light intensity contrast at the nanoscale is sufficient in the case of AuNRs and AuNTs to generate localized polymer parts, while in the case of hexagons and disks, a continuous layer is obtained between the hot spots. Polymerization occurs continuously between two hot spots for the following reasons:

- Diffusion of radicals formed in areas of high $|E|^2$ toward areas of lower $|E|^2$.

- Propagation of radical polymerization initiated in areas of high $|E|^2$ to areas of lower $|E|^2$.

- Diffusion of oxygen (quencher) from areas of low $|E|^2$ to areas of higher $|E|^2$ where it is consumed more rapidly. This effect lowers the polymerization threshold in areas of low $|E|^2$, resulting in homogeneous polymerization over the entire circumference.

On the other hand, the order of Au nanoparticles yielding a higher thickness is as follows: AuNRs > AuNTs> AuNHs> AuNDs. The contours of simulated field intensity show a correlation with the thicknesses of polymer. The electric field intensity follows the order of polymer thicknesses among the four studied shapes. The polymer thickness follows thus the trend exposed in ref 32 but this work also shows that the coupling with photopolymerization makes the quantitative analysis more complex when considering different configurations.

It has been noted that we were not able to correlate precisely the near-field polymerization threshold with the enhancement factor, as it is difficult to detect the polymer layer at very low thicknesses. We thus observe that the near-field polymerization threshold is in the 8.5% - 17.5% range for all nanostructures.

Using AuNTs as an example, we show that we can confine the polymerized zone to a layer less than 10 nm thick with a space of 20 nm. These results go beyond what has been published in the field of high-resolution photopolymerization and open new perspectives in photochemical nanofabrication.

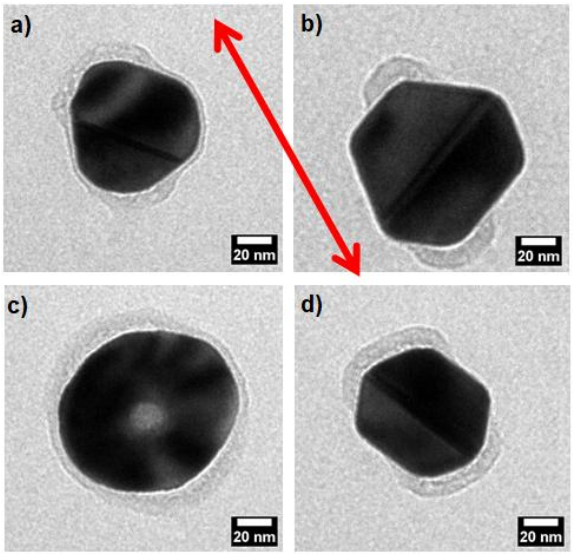

Figure 11: Effect of AuNPs shape on the anisotropy of NF2P, TEM imaging: irradiation at 26.5% D_t. The **red arrow** indicates the polarization of light.

Note that special cases were observed on slightly deformed AuNDs or AuNHs (**Figure 11**). The deformed AuNDs showed NF2P localization (**Figure 11.a** and **Figure 11.c**). For the AuNHs, hexagons with more pronounced tips (smaller curvature radii) were irradiated (**Figure 11.b** and **Figure 11.d**), which allowed a better localization of the NF2P compared to the previously presented AuNHs (**Figure 4**). These results highlight that the presence of a defect in this type of high symmetry NPs makes it possible to induce the localization of the NF2P. This result establishes the link with the results obtained on AuNRs, and also allows us to understand the previous results obtained on nanoparticles prepared by electron beam lithography[30–32]. In the latter case, it is conceivable that the defects on the surface of the NPs and the distorted geometries favor the localization of the field by acting as singularities that

accentuate the field contrast between the direction parallel and perpendicular to the incident polarization, inducing a localization of the polymerization.

Conclusions

In this study, near-field photopolymerization was used as an experimental imaging technique to visualize the electric field distribution around different shapes of colloidally synthesized Au nanoparticles. Through our experimental approach coupled with simulations and using different shapes of AuNPs, it was demonstrated that the localization of near-field photopolymerization is different depending on the type of nano-object used. It was observed that in the case of nanodisks and nanohexagones, contrary to what was expected from the simulation, a homogeneous polymer layer is obtained at the periphery of the NP. On the other hand, for triangles and nanorods, the geometry of the object allows a better localization of the photopolymerization in the near field, this time in agreement with the simulations. These results were interpreted in relation to the field contrast generated by each of the structures, which more or less allows the generation of a chemical contrast from the field distribution. These results contribute to a better understanding of the plasmonic properties of metal nanoparticles and open perspectives for their improvement and future application, in particular for nanofabrication applications.

Supporting Information

Simulated spectra by MNPBEM of NPs; UV-vis spectrum of FBAPO formulation; TEM images of NPs after NFPP for different powers; Electromagnetic field maps and cross sections for AuNRs.

Acknowledgements

O.S, SM, LD, CFD, RB PMA acknowledge ANR for funding (POPCORN grant numbers ANR-19-CE19-0012). This work of the Interdisciplinary Institute HiFunMat, as part of the ITI 2021–2028 program of the University of Strasbourg, CNRS and Inserm, was supported by IdEx Unistra (ANR-10-IDEX-0002) and SFRI (STRAT'US project, ANR-20-SFRI-0012) under the framework of the French Investments for the Future Program. R. B. acknowledges ANR for funding (STRONG-NANO, ANR-22-CE24-0025 and ADVANSPEC, ANR-21-CE42-0006 projects) as well as the Graduate School NANO-PHOT, École Universitaire de Recherche, contract ANR-18-EURE-0013).

References

(1) Lukianova-Hleb, E. Y.; Ren, X.; Sawant, R. R.; Wu, X.; Torchilin, V. P.; Lapotko, D. O. On-Demand Intracellular Amplification of Chemoradiation with Cancer-Specific Plasmonic Nanobubbles. *Nature medicine* **2014**, *20* (7), 778–784.

(2) Yang, X.; Porcel, E.; Marichal, L.; Gonzalez-Vargas, C.; Khitous, A.; Salado-Leza, D.; Li, X.; Renault, J.-P.; Pin, S.; Remita, H.; et al. Human Serum Albumin in the Presence of Small Platinum Nanoparticles. *Journal of Pharmaceutical Sciences* **2024**, *113* (6), 1645-1652. DOI: https://doi.org/10.1016/j.xphs.2024.02.002.

(3) Li, S.; Miao, P.; Zhang, Y.; Wu, J.; Zhang, B.; Du, Y.; Han, X.; Sun, J.; Xu, P. Recent Advances in Plasmonic Nanostructures for Enhanced Photocatalysis and Electrocatalysis. *Advanced Materials* **2021**, *33* (6), 2000086. https://doi.org/10.1002/adma.202000086.

(4) Khitous, A.; Noel, L.; Molinaro, C.; Vidal, L.; Grée, S.; Soppera, O. Sol–Gel TiO2 Thin Film on Au Nanoparticles for Heterogeneous Plasmonic Photocatalysis. *ACS Applied Materials & Interfaces* **2024**, *16* (8), 10856-10866. DOI: 10.1021/acsami.3c15866.

(5) Du, W.; Wang, T.; Chu, H.-S.; Nijhuis, C. A. Highly Efficient On-Chip Direct Electronic–Plasmonic Transducers. *Nature Photonics* **2017**, *11* (10), 623–627.

(6) Linic, S.; Chavez, S.; Elias, R. Flow and Extraction of Energy and Charge Carriers in Hybrid Plasmonic Nanostructures. *Nature Materials* **2021**, *20* (7), 916–924.

(7) Taylor, A. B.; Zijlstra, P. Single-Molecule Plasmon Sensing: Current Status and Future Prospects. *ACS Sens.* **2017**, *2* (8), 1103–1122. https://doi.org/10.1021/acssensors.7b00382.

(8) Khitous, A.; Molinaro, C.; Gree, S.; Haupt, K.; Soppera, O. Plasmon-Induced Photopolymerization of Molecularly Imprinted Polymers for Nanosensor Applications. *Advanced Materials Interfaces* **2023**, 2201651.

(9) Kelly, K. L.; Coronado, E.; Zhao, L. L.; Schatz, G. C. The Optical Properties of Metal Nanoparticles: The Influence of Size, Shape, and Dielectric Environment. *The Journal of Physical Chemistry B*, 2003, *107*, 668–677.

(10) Lalisse, A.; Tessier, G.; Plain, J.; Baffou, G. Quantifying the Efficiency of Plasmonic Materials for Near-Field Enhancement and Photothermal Conversion. *The Journal of Physical Chemistry C* **2015**, *119* (45), 25518–25528.

(11) Khitous, A.; Lin, C.-F.; Kameche, F.; Zan, H.-W.; Malval, J.-P.; Berling, D.; Soppera, O. Plasmonic Au Nanoparticle Arrays for Monitoring Photopolymerization at the Nanoscale. *ACS Applied Nano Materials* **2021**, *4* (9), 8770–8780.

(12) Baffou, G.; Quidant, R.; Girard, C. Heat Generation in Plasmonic Nanostructures: Influence of Morphology. *Applied Physics Letters* **2009**, *94* (15), 153109.

(13) Chatterjee, H.; Rahman, D. S.; Sengupta, M.; Ghosh, S. K. Gold Nanostars in Plasmonic Photothermal Therapy: The Role of Tip Heads in the Thermoplasmonic Landscape. *J. Phys. Chem. C* **2018**, *122* (24), 13082–13094. https://doi.org/10.1021/acs.jpcc.8b00388.

(14) Jia, C.; Li, X.; Xin, N.; Gong, Y.; Guan, J.; Meng, L.; Meng, S.; Guo, X. Interface- Engineered Plasmonics in Metal/Semiconductor Heterostructures. *Advanced Energy Materials* **2016**, *6* (17), 1600431. https://doi.org/10.1002/aenm.201600431.

(15) Lee, J. S.; Han, S.; Shirdel, J.; Koo, S.; Sadiq, D.; Lienau, C.; Park, N. Superfocusing of Electric or Magnetic Fields Using Conical Metal Tips: Effect of Mode Symmetry on the Plasmon Excitation Method. *Optics express* **2011**, *19* (13), 12342–12347.
(16) Montaño-Priede, J. L.; Pal, U. Estimating Near Electric Field of Polyhedral Gold Nanoparticles for Plasmon-Enhanced Spectroscopies. *J. Phys. Chem. C* **2019**, *123* (18), 11833–11839. https://doi.org/10.1021/acs.jpcc.9b01105.
(17) Hasegawa, S.; Imaeda, K.; Imura, K. Plasmon-Enhanced Fluorescence Near Single Gold Nanoplates Studied by Scanning Near-Field Two-Photon Excitation Microscopy. *J. Phys. Chem. C* **2021**, *125* (38), 21070–21076. https://doi.org/10.1021/acs.jpcc.1c06466.
(18) Molinaro, C.; Khitous, A.; Noel, L.; Soppera, O. Nanochemistry by Thermoplasmonic Effects. In *Progress in Nanophotonics 7*; Springer, 2022; pp 71–91.
(19) Kameche, F.; Heni, W.; Telitel, S.; Ge, D.; Vidal, L.; Dumur, F.; Gigmes, D.; Lalevee, J.; Marguet, S.; Douillard, L. Plasmon-Triggered Living Photopolymerization for Elaboration of Hybrid Polymer/Metal Nanoparticles. *Materials Today* **2020**, *40*, 38–47.
(20) Khitous, A.; Molinaro, C.; Thomas, C.; Haupt, K.; Soppera, O. Synthesis and Integration of Hybrid Metal Nanoparticles Covered with a Molecularly Imprinted Polymer Nanolayer by Photopolymerization. *Sensors* **2023**, *23* (8), 3995.
(21) Noel, L.; Khitous, A.; Molinaro, C.; Zan, H.; Berling, D.; Grasset, F.; Soppera, O. Laser Direct Writing of Crystallized TiO_2 by Photothermal Effect Induced by Gold Nanoparticles. *Adv Materials Technologies* **2023**, 2300407. https://doi.org/10.1002/admt.202300407.
(22) Ge, D.; Issa, A.; Jradi, S.; Couteau, C.; Marguet, S.; Bachelot, R. Advanced Hybrid Plasmonic Nano-Emitters Using Smart Photopolymer. *Photonics research* **2022**, *10* (7), 1552–1566.
(23) Aoudjit, T.; Horrer, A.; Kostcheev, S.; Bachelot, R.; Plain, J.; Gérard, D. Photochemical Imaging of Near-Field and Dissymmetry Factor in Chiral Nanostructures. *Advanced Optical Materials* **2023**, *11* (9), 2203015.
(24) Nguyen, M.; Lamouri, A.; Salameh, C.; Lévi, G.; Grand, J.; Boubekeur-Lecaque, L.; Mangeney, C.; Félidj, N. Plasmon-Mediated Chemical Surface Functionalization at the Nanoscale. *Nanoscale* **2016**, *8* (16), 8633–8640.
(25) Kameche, F.; Heni, W.; Telitel, S.; Vidal, L.; Marguet, S.; Douillard, L.; Fiorini-Debuisschert, C.; Bachelot, R.; Soppera, O. Probing Plasmon-Induced Chemical Mechanisms by Free-Radical Nanophotopolymerization. *The Journal of Physical Chemistry C* **2021**, *125* (16), 8719–8731.
(26) Bachelot, R.; H'dhili, F.; Barchiesi, D.; Lerondel, G.; Fikri, R.; Royer, P.; Landraud, N.; Peretti, J.; Chaput, F.; Lampel, G. Apertureless Near-Field Optical Microscopy: A Study of the Local Tip Field Enhancement Using Photosensitive Azobenzene-Containing Films. *Journal of Applied Physics* **2003**, *94* (3), 2060–2072.
(27) Hubert, C.; Rumyantseva, A.; Lerondel, G.; Grand, J.; Kostcheev, S.; Billot, L.; Vial, A.; Bachelot, R.; Royer, P.; Chang, S.; Gray, S. K.; Wiederrecht, G. P.; Schatz, G. C. Near-Field Photochemical Imaging of Noble Metal Nanostructures. *Nano Lett.* **2005**, *5* (4), 615–619. https://doi.org/10.1021/nl047956i.
(28) Lefin, P.; Fiorini, C.; Nunzi, J.-M. Anisotropy of the Photoinduced Translation Diffusion of Azo-Dyes. *Optical Materials* **1998**, *9* (1–4), 323–328.
(29) Yang, P.; Zheng, J.; Xu, Y.; Zhang, Q.; Jiang, L. Colloidal Synthesis and Applications of Plasmonic Metal Nanoparticles. *Advanced Materials* **2016**, *28* (47), 10508–10517. https://doi.org/10.1002/adma.201601739.
(30) Tijunelyte, I.; Kherbouche, I.; Gam-Derouich, S.; Nguyen, M.; Lidgi-Guigui, N.; de la Chapelle, M. L.; Lamouri, A.; Lévi, G.; Aubard, J.; Chevillot-Biraud, A. Multi-

Functionalization of Lithographically Designed Gold Nanodisks by Plasmon-Mediated Reduction of Aryl Diazonium Salts. *Nanoscale Horizons* **2018**, *3* (1), 53–57.
(31) Ibn-El-Ahrach, H.; Bachelot, R.; Lerondel, G.; Vial, A.; GRIMAULT, A.-S.; Plain, J.; Royer, P.; Soppera, O. Controlling the Plasmon Resonance of Single Metal Nanoparticles by Near-Field Anisotropic Nanoscale Photopolymerization. *Journal of microscopy* **2008**, *229* (3), 421–427.
(32) Ge, D.; Marguet, S.; Issa, A.; Jradi, S.; Nguyen, T. H.; Nahra, M.; Béal, J.; Deturche, R.; Chen, H.; Blaize, S. Hybrid Plasmonic Nano-Emitters with Controlled Single Quantum Emitter Positioning on the Local Excitation Field. *Nature Communications* **2020**, *11* (1), 3414.
(33) Mitiche, S.; Marguet, S.; Charra, F.; Douillard, L. Plasmonics of Regular Shape Particles, a Simple Group Theory Approach. *Nano Res.* **2020**, *13* (6), 1597–1603. https://doi.org/10.1007/s12274-020-2776-y.
(34) Jégat, C.; Rollin, E.; Douillard, L.; Soppera, O.; Nakatani, K.; Laurent, G. Patterning Gold Nanorod Assemblies by Deep-UV Lithography. *The Journal of Physical Chemistry C* **2022**, *126* (32), 13729–13738.
(35) Ye, X.; Zheng, C.; Chen, J.; Gao, Y.; Murray, C. B. Using Binary Surfactant Mixtures to Simultaneously Improve the Dimensional Tunability and Monodispersity in the Seeded Growth of Gold Nanorods. *Nano letters* **2013**, *13* (2), 765–771.
(36) Li, B.; Lalevée, J.; Mazur, L. M.; Matczyszyn, K.; Ravaine, S.; Jradi, S. Copper Complex-Based Photoinitiator for High Resolution Two-Photon Polymerization. *Additive Manufacturing* **2023**, *75*, 103741.
(37) Waxenegger, J.; Trügler, A.; Hohenester, U. Plasmonics Simulations with the MNPBEM Toolbox: Consideration of Substrates and Layer Structures. *Computer Physics Communications* **2015**, *193*, 138–150.
(38) Hohenester, U.; Trügler, A. MNPBEM–A Matlab Toolbox for the Simulation of Plasmonic Nanoparticles. *Computer Physics Communications* **2012**, *183* (2), 370–381.
(39) Luke, K.; Okawachi, Y.; Lamont, M. R.; Gaeta, A. L.; Lipson, M. Broadband Mid-Infrared Frequency Comb Generation in a Si 3 N 4 Microresonator. *Optics letters* **2015**, *40* (21), 4823–4826.
(40) Johnson, P. B.; Christy, R. W. Optical Constants of the Noble Metals. *Phys. Rev. B* **1972**, *6* (12), 4370–4379. https://doi.org/10.1103/PhysRevB.6.4370.
(41) Deeb, C.; Ecoffet, C.; Bachelot, R.; Plain, J.; Bouhelier, A.; Soppera, O. Plasmon-Based Free-Radical Photopolymerization: Effect of Diffusion on Nanolithography Processes. *Journal of the American Chemical Society* **2011**, *133* (27), 10535–10542.
(42) Blandre, E.; Jalas, D.; Petrov, A. Yu.; Eich, M. Limit of Efficiency of Generation of Hot Electrons in Metals and Their Injection inside a Semiconductor Using a Semiclassical Approach. *ACS Photonics* **2018**, *5* (9), 3613–3620. https://doi.org/10.1021/acsphotonics.8b00473.
(43) Khitous, A.; Lartigue, L.; Moreau, J.; Soppera, O. Insights into Photopolymerization at the Nanoscale Using Surface Plasmon Resonance Imaging. *Small* **2024**, 2401885. https://doi.org/10.1002/smll.202401885.
(44) Li, J.; Cushing, S. K.; Meng, F.; Senty, T. R.; Bristow, A. D.; Wu, N. Plasmon-Induced Resonance Energy Transfer for Solar Energy Conversion. *Nature Photonics* **2015**, *9* (9), 601–607.
(45) Chegel, V.; Whitcombe, M. J.; Turner, N. W.; Piletsky, S. A. Deposition of Functionalized Polymer Layers in Surface Plasmon Resonance Immunosensors by In-Situ Polymerization in the Evanescent Wave Field. *Biosensors and Bioelectronics* **2009**, *24* (5), 1270–1275.

(47) Zhou, X.; Wenger, J.; Viscomi, F. N.; Le Cunff, L.; Béal, J.; Kochtcheev, S.; Yang, X.; Wiederrecht, G. P.; Colas des Francs, G.; Bisht, A. S. Two-Color Single Hybrid Plasmonic Nanoemitters with Real Time Switchable Dominant Emission Wavelength. *Nano letters* **2015**, *15* (11), 7458–7466.
(48) Awada, C.; Popescu, T.; Douillard, L.; Charra, F.; Perron, A.; Yockell-Lelièvre, H.; Baudrion, A.-L.; Adam, P.-M.; Bachelot, R. Selective Excitation of Plasmon Resonances of Single Au Triangles by Polarization-Dependent Light Excitation. *J. Phys. Chem. C* **2012**, *116* (27), 14591–14598. https://doi.org/10.1021/jp303475c.

TOC Graphic